Progress In Electromagnetics Research C, Vol. 115, 145–160, 2021

Design and Modelling of Ladder-Shape Topology Generating Bandpass NGD Function

Samuel Ngoho[1, *], Yves C. M. Boussougou[2], Syed S. Yazdani[3], Yuandan Dong[4], Nour M. Murad[5], Sébastien Lalléchère[6], Wenceslas Rahajandraibe[7], and Blaise Ravelo[8]

Abstract—This paper introduces a model and design of an innovative bandpass (BP) negative group delay (NGD) distributed circuit. The passive circuit topology under study is constituted by fully distributed elements without lumped components. The NGD passive structure is implemented as a ladder shape topology composed of distributed transmission line (TL) elements. The S-matrix model is established from TL-based equivalent Z-matrix operations with respect to the ladder geometry. As a proof of concept, a two-cell ladder prototype is designed in microstrip technology, which is simulated, fabricated, and tested. The calculated and simulated measurements are in very good agreement with the validation of BP NGD behaviour. NGD value is better than -3 ns with centre frequency between 3.56 and 3.68 GHz over more than 30 MHz NGD bandwidth being observed. The circuit operates under insertion loss better than 5 dB and reflection loss better than 8 dB. This innovative BP NGD passive circuit can be useful in the RF and microwave engineering area, for example, to reduce the signal propagation delay in the upcoming and 5G telecommunication systems.

1. INTRODUCTION

To satisfy the public demands and industrial needs in terms of speed and data rate, the evolution of communication systems is growing exponentially with billions of connected objects constituting diverse infrastructures of big smart urban cities [1–3]. This intensive and deep integration of devices accompanied with the increase of operating frequencies would not have been achieved without critical issues on signal delay and integrity as the signal is conveyed by and through miniaturized components and relatively complex interconnects on a single chip most often multilayered and multi functions. Moreover, electromagnetic compatibility problems between integrated circuits and the associated electrical connections have to be considered with more attention during the design and implementation phases. The 5G communication technology presents a typical example where the signal delay will be a master key of performance as it aims to target Ultra-Reliable Low Latency Communications (URLLC) [1]. Therefore, the reduction of such issues remains an innovative research work for the future communication systems [4] in order to guarantee the time propagation and integrity of the signal. We can emphasize more and more influences of group delay (GD) [5, 6] in the microwave electronics systems since the passive RLC circuit networks are not appropriate for the increase of the operational frequencies. Research works are performed on reducing the signal delay, flatting the band pass filter

Received 16 May 2021, Accepted 26 July 2021, Scheduled 13 September 2021

* Corresponding author: Samuel Ngoho (samngoho@yahoo.fr).
[1] Association Française de Science des Systèmes (AFSCET), Paris, France. [2] Laboratoire des Mathématiques et Physique Appliqués (LMPA), Ecole Polytechnique de Masuku, Université des Sciences et Techniques de Masuku, Gabon. [3] Software Engineering Department, Bahria University Karachi Campus, Karachi 75260, Pakistan. [4] School of Electronic Science and Technology, University of Electronic Science and Technology of China, China. [5] Energy Lab, Network and Telecom Team, Institut Universitaire de Technologie, University of La Reunion, Saint Denis 97715, France. [6] Université Clermont Auvergne (UCA), CNRS, SIGMA Clermont, Institut Pascal, Aubière, France. [7] Aix-Marseille University, CNRS, University of Toulon, IM2NP UMR7334, Marseille, France.
[8] Nanjing University of Information Science & Technology (NUIST), Nanjing 210044, Jiangsu, China.

response, or the phase linearity [7–10]. The first studies and investigations of the negative group delay (NGD) function were carried out on the light pulse propagation in a dispersive medium. Inside an absorption line, it was theoretically shown that a light pulse velocity propagated at group velocities faster than the speed of light in a vacuum, which can become negative as experienced later with left-handed matematerial periodical structures [11, 12]. Some promising experiences have been achieved in the field of RF/microwave systems to solve these issues. To reduce the interconnect delay and improve the signal integrity, repeaters were designed and inserted in certain integrated circuits [13]. Alternative innovative solution of delay reduction based on negative group delay (NGD) equalization method was proposed [14, 15]. It is noteworthy to highlight that the NGD solution enables preservation of the signal quality without affecting the information speed. The NGD function was innovatively implemented within microwave circuits [15] as antenna [16, 17] and sensor [18–20] performances by using negative refractive index resonant metamaterials, antenna beamformer [21, 22], non-Foster network designing [23], and independent frequency NGD phase shifter [24]. Analytical modeling of transmission line (TL) and electrical interconnects were developed [25]. Nevertheless, the NGD function remains, so far, unknown and unfamiliar to most microwave design research engineers. This research work aims to democratize with the simplest academic way the NGD function. Doing this, the analogical theory between filter and NGD behavior were suggested [26, 27]. Subsequently, the concept of bandpass (BP) NGD function was introduced [26, 27]. This type of BP NGD circuit is currently the most developed by NGD researchers [9–12, 28–39] for targeting especially the RF and microwave engineering. The few research groups around the world, working on NGD microwave design, have demonstrated the outstanding diversity of NGD aspects as compared to, for example, active resonator based distributed circuits [9], effective negative refractive index TL [11, 12], defected ground structure [30], coupled line based structures [31, 32], compact self-matched TLs [33, 34], asymmetrical directional coupler [38], and transversal filter approach [39]. During the last decade, significant effort has been spent for the development of compact distributed NGD circuits [34, 35]. Among those diverse topologies, we pay particular attention to hybrid coupler-based BP NGD topology which was not, until now, sufficiently exploited [36, 37]. Analytical formulations of NGD synthesizer using feedback hybrid coupler were proposed in [36, 37]. But intuitively, slight modifications of this topology should enable the design of BP NGD function operating in microwave engineering frequencies.

Because of the lumped-based circuits operating frequency band and the complexity of the distributed microstrip circuits, continuous research works are necessary to find a good tradeoff design of BP NGD topologies. In the present study, by inspiring and modifying the hybrid coupler topology, we propose a simple BP NGD topology constituted by a ladder geometrical shape structure. The innovative NGD structures should be designed with available technology enabling both simulated and experimental investigations. For this reason, a distributed microstrip line is chosen to design and implement the good compromise BP NGD topology under study.

For the better understanding, the paper is organized in four main sections as follows. Section 2 will define the main specifications of BP NGD function. The basic parameters for the BP NGD function qualification will be described. The NGD BP ladder-shape topology will be presented and analytically modeled in Section 3. The topological algebra based on Z-matrix operations will be elaborated to establish the equivalent S-matrix. The proof-of-concept (POC) design and validation of BP NGD function with two-cell ladder-shape microstrip circuit will be discussed in Section 4. Parametric analyses with respect to the ladder circuit physical widths and lengths will be introduced for assessing their impact on the BP NGD characteristics. Then, Section 5 will be the conclusion of the paper.

2. RECALL ON THE BP NGD SPECIFICATIONS

A preliminary definition of BP NGD function is introduced in the present section. After recalling the theoretical expression, the specification parameters will be defined.

2.1. S-Matrix Modelling for NGD Analysis

First and foremost, acting as a two-port system, the NGD circuit investigated in this paper can be generalized by the black box system represented by Fig. 1(a).

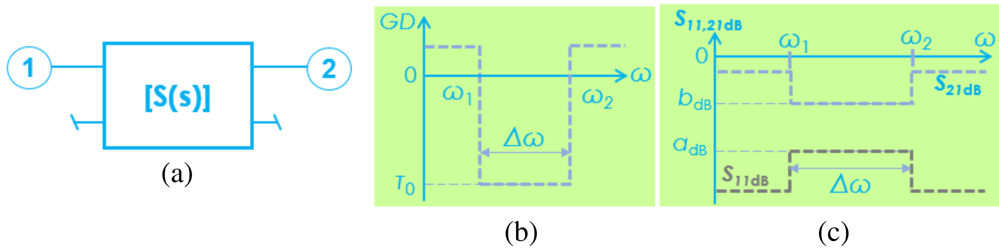

Figure 1. (a) Two-port black box microwave system. BP NGD function ideal specifications: (b) GD, and (c) S-parameters, S_{11} and S_{21}.

By denoting $s = j\omega$, the complex angular frequency variable, this symmetrical system can be analytically modelled by the 2-D S-matrix:

$$[S(j\omega)] = \begin{bmatrix} S_{11}(j\omega) & S_{21}(j\omega) \\ S_{21}(j\omega) & S_{11}(j\omega) \end{bmatrix} \tag{1}$$

because $S_{11} = S_{22}$ and $S_{12} = S_{21}$. In comparison to the classical RF and microwave circuits, the NGD study requires further analysis of frequency responses of S-matrix introduced in Equation (1). Before the analytical definition, it is worth to note that this paper is essentially focused on a passive circuit. Therefore, the NGD circuit performance must include:

- The input and output reflection losses are related to the reflection coefficient magnitudes which must be lower than an expected matching value, $a < 1$:

$$\begin{cases} S_{11}(\omega) = |S_{11}(j\omega)| \leq a \\ S_{22}(\omega) = |S_{22}(j\omega)| \leq a \end{cases} \tag{2}$$

- The insertion loss or gain related to the transmission coefficient magnitude should be greater than an expected value, $b < 1$:

$$S_{21}(\omega) = |S_{21}(j\omega)| \geq b \tag{3}$$

According to the description, the NGD study fundamentally depends on the GD analytical expression. For this reason, it would be important to recall the mathematical definition of this key parameter. The GD is derived from the phase of the transmission coefficient of S-matrix introduced in Equation (1). The analytical model of the associated GD is defined by:

$$\mathrm{GD}(\omega) = -\partial \arg\left[S_{21}(j\omega)\right] / \partial\omega. \tag{4}$$

2.2. Graphical Specifications of BP NGD Function

The analysis of unfamiliar BP NGD function was inspired from BP filter response [26, 27]. However, different from the classical filter theory with the characterization based on the S_{21} magnitude behaviour, the NGD function characterization depends essentially on the sign of GD expressed in Equation (4). By taking $\omega_{m=1,2} = 2\pi f_m$, the type of NGD function depends on the frequency band position, $\omega_1 \leq \omega \leq \omega_2$, where we have:

$$\mathrm{GD}(\omega_1 \leq \omega \leq \omega_2) \leq 0. \tag{5}$$

Figure 1(b) illustrates an ideal GD response of BP NGD function. The specifications related to the GD response are defined as follows. By taking a real negative delay, τ_0, the GD value, NGD bandwidth, respectively:

$$\mathrm{GD}(\omega_1 \leq \omega \leq \omega_2) = \tau_0 < 0 \tag{6}$$

$$\Delta\omega = 2\pi\Delta f = \omega_2 - \omega_1 \tag{7}$$

and NGD centre frequency, $\omega_0 = 2\pi f_0 \in [\omega_1, \omega_2]$. Moreover, as illustrated in Fig. 1(c), the reflection and transmission coefficients of ideal BP NGD function can be specified by:

$$\begin{cases} S_{11}(\omega_1 \leq \omega \leq \omega_2) = S_{11}(\omega) = a \\ S_{21}(\omega_1 \leq \omega \leq \omega_2) = S_{22}(\omega) = b \end{cases}. \tag{8}$$

3. *S*-MATRIX MODEL OF LADDER SHAPE CELL TOPOLOGY

The present section develops the ladder TL topology S-matrix model. First, the TL element-model will be described. The reduction mechanism of the structure Z-matrix will be established, and consequently the equivalent S-matrix is extracted.

3.1. TL-Based Topological Description

Figure 3 introduces the equivalent circuit of the ladder shape topology. It consists of two meshes of cells. The main access ports, ① and ②, are connected to nodes M_1 and M_2. On the left side, we have the TL connected to nodes M_1 and M_a. Conversely, on the right side, we have the connections between nodes M_2 and M_b. The symmetric axis of the ladder is connected to the intermediate nodes M_c and M_d. The two-port circuit is constituted by seven pieces of elementary TLs, denoted by $\mathrm{TL}_x(Z_x, \gamma_x)$ (the subscript is $x = a, b$) which is defined by the characteristic impedance, Z_x, and the constant propagation is defined by:

$$\gamma_x(j\omega) = \alpha_x(\omega) + j\beta_x(\omega) \tag{9}$$

where $\alpha_x(\omega)$ and $\beta_x(\omega)$ are the attenuation and phase constant.

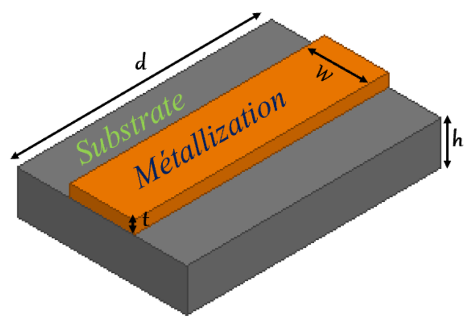

Figure 2. Typical microstrip line and geometrical parameters.

In the following section, these TL electrical characteristics are extracted from the microstrip case TL physical parameters by using Hammerstad-Jensen model [40] in which some equations are expressed below. The effective permittivity and t characteristic impedance of the microstrip line are defined by:

$$\varepsilon_{\mathit{eff}} \approx 0.5 \left\{ e_r + 1 + (e_r - 1) \left[0.04 \left(1 - \frac{w}{h}\right)^2 + \frac{1}{\sqrt{1 + 12\frac{h}{w}}} \right] \right\}; \tag{10}$$

$$Z_c \approx \frac{Z_{air}}{2\pi\sqrt{\varepsilon_{\mathit{eff}}}} + \ln\left(\frac{5.98h}{w+t}\right) \tag{11}$$

with $w \ll h$. w, t, and h are respectively the width, thickness of the conductive metallized electrode and the height of the substrate as illustrated in Fig. 2. Z_{air} represents the characteristic impedance of the line in vacuum. This characteristic impedance is defined as:

$$Z_{air} \approx \sqrt{\frac{\mu_0}{\varepsilon_0}} \tag{12}$$

where μ_0 and ε_0 are the vacuum permeability and permittivity, respectively. The wave speed, phase constant, and wavelength are expressed as:

$$v = \frac{c}{\sqrt{e_{\mathit{eff}}}} \tag{13}$$

$$\beta(w) = \frac{2\pi}{\lambda(w)} \tag{14}$$

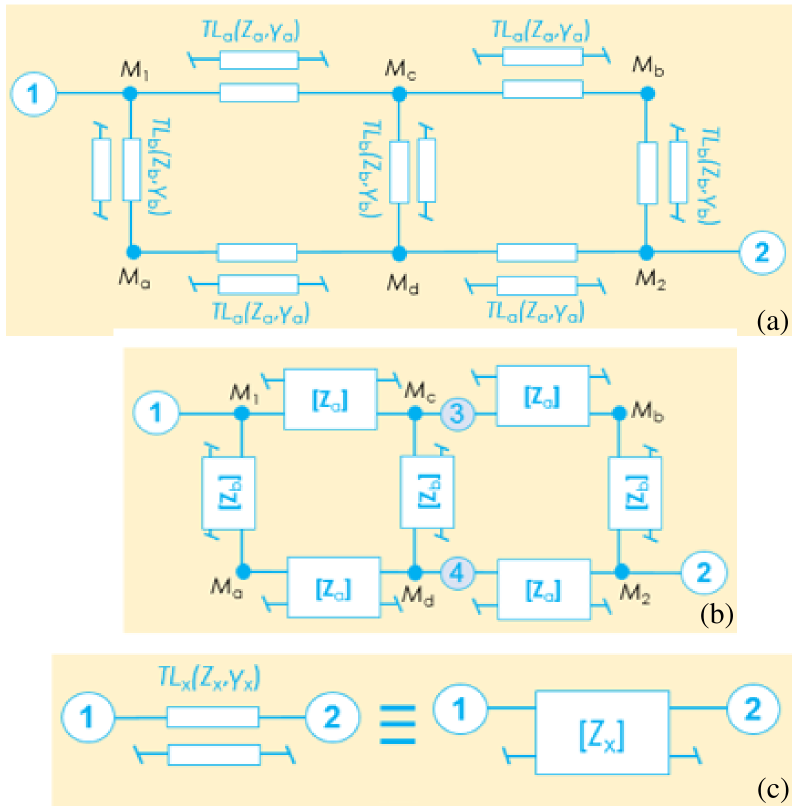

Figure 3. (a) TL based topology of ladder network under study, (b) two-port TL Z-matrix blocks-based equivalent diagram, and (c) TL and its two-port Z-matrix equivalent model.

$$\lambda(w) = \frac{2\pi v}{w} \tag{15}$$

The initial step of the S-matrix modelling of the ladder topology starts with the consideration of the equivalent impedance matrix or Z-matrix of each elementary TL $\mathrm{TL}_x(Z_x, \gamma_x)$. Fig. 3(c) illustrates the two-port black box representation of this TL. The TL_x physical lengths are assumed equal to $d_{x=a,b}$. According to the TL theory, the equivalent Z-matrix of TL_x can be written as:

$$[Z_x(j\omega)] = \begin{bmatrix} Z_1(j\omega) & Z_2(j\omega) \\ Z_2(j\omega) & Z_1(j\omega) \end{bmatrix} \tag{16}$$

with:

$$\begin{cases} Z_1(j\omega) = Z_x/\tanh\left[\gamma_x(\omega)d\right] \\ Z_2(j\omega) = Z_x/\sinh\left[\gamma_x(\omega)d\right] \end{cases}. \tag{17}$$

This expression will be exploited in the following paragraphs to determine the analytical model of the ladder Z-matrix impedance.

3.2. Z-Matrix Operation for Determining the Ladder Shape Analytical Model

Before the analytical elaboration, we can redraw the diagram with the elementary Z-matrix defined previously. Fig. 3(b) introduces the equivalent diagram of the ladder circuit constituted by the TL_x Z-matrices. We can identify, in this diagram, the different nodes, $M_{1,2,a,b,c,d}$, of the initial circuit introduced in Fig. 3(a). The main access ports are referenced by nodes ① and ②. The intermediate ports are represented by nodes ③ and ④. With these port references, we can proceed towards the reduction of this topology. The splitting of the previous diagram enables us to express the partial block diagram. The left and right parts which are equivalent subsystem of the ladder diagram are presented

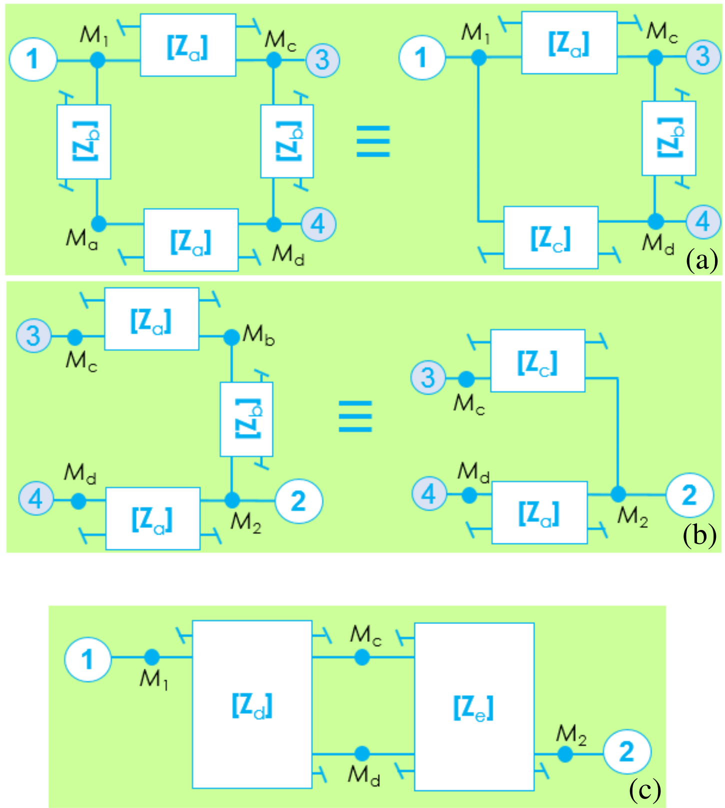

Figure 4. Reduced topology of (a) left and (b) right parts of the ladder network equivalent diagrams, and (c) 3-port S-matrix block diagram-based ladder network equivalent schematic.

in Fig. 4(a) and Fig. 4(b), respectively. The system theory enables us to reduce this diagram with combination of lateral Z-matrices, $[Z_a]$, and $[Z_b]$, between the nodes M_1M_c and M_1M_a, respectively, as illustrated in Fig. 4(a). A similar algebraic operation is performed for the lateral branch between the nodes M_2M_d and M_cM_d, as explained in Fig. 4(b).

For both parts of the diagram, the equivalent two-port Z-matrix, $[Z_c]$, is expressed as:

$$[Z_c(j\omega)] = \frac{\begin{bmatrix} x_1(j\omega) & Z_{2a}(j\omega)Z_{2b}(j\omega) \\ Z_{2a}(j\omega)Z_{2b}(j\omega) & x_2(j\omega) \end{bmatrix}}{Z_{1a}(j\omega) + Z_{1b}(j\omega)} \tag{18}$$

with:

$$\begin{cases} x_1(j\omega) = Z_{1a}^2(j\omega) - Z_{2a}^2(j\omega) + Z_{1a}(j\omega)Z_{1b}(j\omega) \\ x_2(j\omega) = Z_{1b}^2(j\omega) - Z_{2b}^2(j\omega) + Z_{1a}(j\omega)Z_{1b}(j\omega) \end{cases}. \tag{19}$$

After this first level of Z-matrix reduction, we can proceed towards the analytical calculation of the three-port equivalent matrix of the different parts. Accordingly, we can represent the left part of the ladder topology as a three-port block. This block is equivalent to the 3-D Z-matrix:

$$[Z_d(j\omega)] = \frac{\begin{bmatrix} \zeta_1(j\omega) & \xi_1(j\omega) & \xi_2(j\omega) \\ \xi_1(j\omega) & \zeta_2(j\omega) & \xi_3(j\omega) \\ \xi_2(j\omega) & \xi_3(j\omega) & \zeta_3(j\omega) \end{bmatrix}}{2Z_{1a}(j\omega)\left[Z_{1a}(j\omega) + Z_{1b}(j\omega)\right] - Z_{2a}^2(j\omega)} \tag{20}$$

with:

$$\begin{cases} \zeta_1(j\omega) = Z_{1a}(j\omega)\left[Z_{1a}^2(j\omega) + Z_{1a}(j\omega)Z_{1b}(j\omega) - Z_{2a}^2(j\omega)\right] \\ \zeta_2(j\omega) = 2Z_{1a}(j\omega)\left[Z_{1a}(j\omega)Z_{1b}(j\omega) + Z_{1b}^2(j\omega) - Z_{2b}^2(j\omega)\right] - Z_{2a}^2(j\omega)Z_{1b}(j\omega) \\ \zeta_3(j\omega) = 2Z_{1a}(j\omega)\left[Z_{1a}^2(j\omega) + Z_{1a}(j\omega)Z_{1b}(j\omega) - Z_{1b}^2(j\omega)\right] - Z_{2a}^2(j\omega)Z_{1b}(j\omega) \end{cases} \quad (21)$$

$$\begin{cases} \xi_1(j\omega) = Z_{1a}(j\omega)Z_{1b}(j\omega)Z_{2b}(j\omega) \\ \xi_2(j\omega) = Z_{2a}(j\omega)\left[Z_{1a}^2(j\omega) + Z_{1a}(j\omega)Z_{1b}(j\omega) - Z_{2a}^2(j\omega)\right] \\ \xi_3(j\omega) = Z_{2a}^2(j\omega)Z_{2b}(j\omega) \end{cases}. \quad (22)$$

Similarly, the right part is equivalent to the three-dimension Z-matrix:

$$[Z_e(j\omega)] = \frac{\begin{bmatrix} y_1(j\omega) & Z_{1b}(j\omega)Z_{2a}(j\omega) & Z_{1b}(j\omega)Z_{2b}(j\omega) \\ Z_{1b}(j\omega)Z_{2a}(j\omega) & y_2(j\omega) & Z_{1a}(j\omega)Z_{2b}(j\omega) \\ Z_{1b}(j\omega)Z_{2b}(j\omega) & Z_{1a}(j\omega)Z_{2b}(j\omega) & y_3(j\omega) \end{bmatrix}}{2\left[Z_{1a}(j\omega) + Z_{1b}(j\omega)\right]} \quad (23)$$

with:

$$\begin{cases} y_1(j\omega) = Z_{1a}(j\omega)\left[Z_{1a}(j\omega) + Z_{1b}(j\omega)\right] - Z_{1b}^2(j\omega) \\ y_2(j\omega) = \dfrac{\left\{\begin{array}{l} Z_{1a}^2(j\omega)\left[Z_{1a}(j\omega)\left[2Z_{1b}^2(j\omega) - Z_{2b}^2(j\omega)\right] + 2Z_{1b}(j\omega)\left[Z_{1b}^2(j\omega) - Z_{2b}^2(j\omega)\right]\right] \\ +Z_{1b}^2(j\omega)Z_{2a}(j\omega)\left[Z_{2a}(j\omega)\left[Z_{2a}(j\omega) - 2Z_{1a}(j\omega)\right] + Z_{2b}^2(j\omega)\right] \end{array}\right\}}{Z_{1a}(j\omega)\left[Z_{1b}(j\omega)\left[Z_{1a}(j\omega) + Z_{1b}(j\omega)\right] - Z_{2b}^2(j\omega)\right] - Z_{2a}^2(j\omega)Z_{1b}(j\omega)} \\ y_3(j\omega) = Z_{1b}(j\omega)\left[Z_{1a}(j\omega) + Z_{1b}(j\omega)\right] - Z_{2b}^2(j\omega) \end{cases} \quad (24)$$

3.3. General Expression of Ladder-Shape Topology *Z*- and *S*-Matrices

Figure 4(c) represents the reduced diagram of the ladder subsystem. The new diagram is composed of the combination of 3-D Z-matrices constituting three-port left and right parts. The linear algebraic operation allows to reduce this diagram. Therefore, we can demonstrate analytically the expression of the general two-port block diagram introduced in Fig. 4(c). Subsequently, knowing that $Z_{d_{mn}}(j\omega) = Z_{d_{nm}}(j\omega)$, and $Z_{e_{mn}}(j\omega) = Z_{e_{nm}}(j\omega)$ for $m \neq n$ which belongs to $\{1, 2, 3\}$, the equivalent two-dimension Z-matrix is expressed as:

$$[Z_{ngd}(j\omega)] = \begin{bmatrix} Z_{1ngd}(j\omega) & Z_{2ngd}(j\omega) \\ Z_{2ngd}(j\omega) & Z_{1ngd}(j\omega) \end{bmatrix} \quad (25)$$

where:

$$Z_{1ngd}(j\omega) = \frac{\left\{\begin{array}{l} Z_{d11}(j\omega)\left[\left[Z_{d22}(j\omega)+Z_{e22}(j\omega)\right]\left[Z_{d33}(j\omega)+Z_{e33}(j\omega)\right] - Z_{e23}^2(j\omega)\right] \\ -Z_{d13}^2(j\omega)\left[Z_{d22}(j\omega)+Z_{e22}(j\omega)\right] - Z_{d11}(j\omega)Z_{d23}(j\omega)\left[Z_{d23}(j\omega)+2Z_{e23}(j\omega)\right] + Z_{d12}(j\omega) \\ \left[Z_{d13}(j\omega)\left[Z_{d23}(j\omega)+Z_{e23}(j\omega)\right] - Z_{d12}(j\omega)\left[Z_{d33}(j\omega) + Z_{e33}(j\omega)\right]\right] \end{array}\right\}}{D(j\omega)} \quad (26)$$

$$Z_{2ngd}(j\omega) = \frac{\left\{\begin{array}{l} Z_{d13}(j\omega)\left[Z_{e13}(j\omega)\left[Z_{d22}(j\omega) + Z_{e22}(j\omega)\right] - Z_{e12}(j\omega)\left[Z_{d23}(j\omega) + Z_{e23}(j\omega)\right]\right] \\ +Z_{d12}(j\omega)\left[Z_{e12}(j\omega)\left[Z_{d12}(j\omega) + Z_{d33}(j\omega)\right] - Z_{e13}(j\omega)\left[Z_{d23}(j\omega) + Z_{d23}(j\omega)\right]\right] \end{array}\right\}}{D(j\omega)} \quad (27)$$

where:

$$D(j\omega) = \left[Z_{d22}(j\omega)+Z_{e22}(j\omega)\right] - Z_{e23}^2(j\omega) + \left[Z_{d33}(j\omega)+Z_{e33}(j\omega)\right] - Z_{d23}(j\omega)\left[Z_{d23}(j\omega)+Z_{e23}(j\omega)\right]. \quad (28)$$

The equivalent global S-matrix can be derived from Z-to-S transform relationship [41]:

$$[S(j\omega)] = \left([Z_{ngd}(j\omega)] - \begin{bmatrix} R_0 & 0 \\ 0 & R_0 \end{bmatrix}\right) \times \left([Z_{ngd}(j\omega)] + \begin{bmatrix} R_0 & 0 \\ 0 & R_0 \end{bmatrix}\right)^{-1}. \quad (29)$$

$R_0 = 50\,\Omega$. Consequently, the ladder network reflection and transmission coefficients of S-matrix model introduced in Equation (1) are expressed as:

$$S_{11}(j\omega) = \frac{Z_{1ngd}(j\omega) - Z_{2ngd}(j\omega) - R_0}{R_0 + Z_{1ngd}(j\omega) + Z_{2ngd}(j\omega)} \tag{30}$$

$$S_{21}(j\omega) = \frac{2Z_{1ngd}(j\omega)}{R_0 + Z_{1ngd}(j\omega) + Z_{2ngd}(j\omega)}. \tag{31}$$

The GD of the ladder network is computed from this transmission coefficient by means of Equations (4)–(5).

3.4. Design Approach of the BP NGD Ladder Shape Circuit

Similar to the classical microwave passive circuits as filter, power divider/combiner, coupler, the design approach of NGD circuit can be performed following a design guide. For example, the design of the BP NGD ladder circuit under study can be performed under the following steps (S_n, $n \in \{1, 2, 3, 4, 5, 6\}$) diagram on Fig. 5. The feasibility of the developed S-matrix model and NGD design approach (see previous steps 1–7) is verified, and a POC will be presented in the next section.

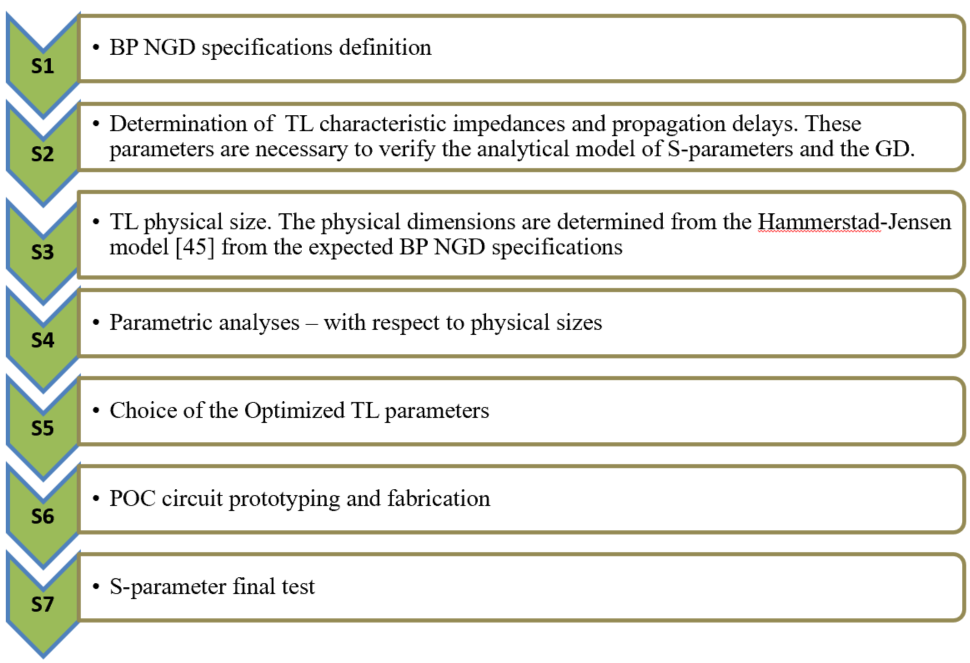

Figure 5. Steps diagram design of the Ladder-shaped topology.

The NGD specifications are based on the graphical responses of Fig. 1(b) and Fig. 1(c). In this paper, the following specifications are defined: $f_0 = 3.6\,\text{GHz}$, $\text{GD}(f_0) = -3\,\text{ns}$, and $\Delta f = 30\,\text{MHz}$. The physical dimensions were determined from the Hammerstad-Jensen model [40] from the expected BP NGD specifications by means of the NGD center frequency, characteristic impedances, and the electrical lengths.

4. VALIDATION RESULTS

This section is focused on the BP NGD validation of the previously theorized ladder shape topology. After the POC description, parametric analyses with respect to the circuit physical sizes will be elaborated. Then, the BP NGD responses from theoretical calculations based on S-parameters model are presented in Eqs. (24) and (25), simulations from commercial tool ADS® from Keysight Technologies®, and measurement will be compared and discussed.

4.1. Ladder Circuit Design and POC Description

Figure 6(a) presents the ADS® design of the two-cell ladder circuit parametrically analyzed. The circuit is made up of 4 identical elements of horizontal TL, TL_1, and three identical elements of vertical TL, TL_2. $TL_m = 1, 2$ is characterized by physical width, w_m, and length, d_m. The 3-D design of the two-cell ladder circuit implemented in microstrip technology is shown in Fig. 6(b) with port ① and port ② having main accesses. The POC circuit physical and electrical parameters are summarized in Table 1.

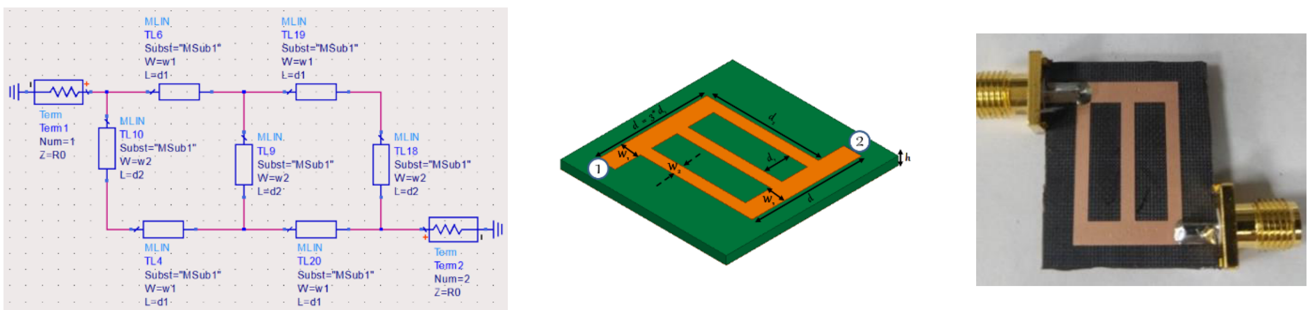

(a) (b) (c)

Figure 6. Ladder shape circuit prototype: (a) ADS® schematic, (b) 3-D design and (c) photograph.

Table 1. Physical parameters of the ladder prototype introduced in Fig. 4.

Type	Description	Name	Value
Ladder	Length	d_1	$3\,\text{mm} \to 4.5\,\text{mm}$
		d_2	$14\,\text{mm} \to 15\,\text{mm}$
	Width	w_1	$2\,\text{mm} \to 3\,\text{mm}$
		w_2	$1\,\text{mm} \to 2\,\text{mm}$
F4BK 350 substrate	Relative permittivity	ε_r	3.5
	Loss tangent	$\tan(\delta)$	0.001
	Height	h	1.27 mm
Metallization	Thickness	t	35 µm
	Conductivity	σ	58 MS/s

4.2. Physical Width and Length Parametric Analyses

The parametric analyses consist of evaluating the influences of ladder circuit TL physical parameters on the BP NGD response. The analyses are based on the S-parameter simulations from 3 GHz to 4 GHz with the commercial tool ADS® from Keysight Technologies®.

4.2.1. Parametric Analysis with Respect to w_1

Figure 7 presents the GD, S_{21}, and S_{11} cartographies of the structure shown in Fig. 6 in function of w_1 and frequency, f. In this case, w_1 varies from 2 mm to 3 mm by 0.1 mm-step. Fig. 7(a) shows a BP NGD behavior in the considered range of w_1. Furthermore, as depicted in Fig. 7(d), the NGD value increases when w_1 varies from 2 mm to 2.7 mm, and it decreases when w_1 varies from 2.7 mm to 3 mm. The NGD bandwidth, Δf, is about 10.2 MHz for each w_1 value. Moreover, the NGD center frequency increases with frequency step less than 8 MHz. Fig. 7(b) highlights that S_{21} mapping behaves as the

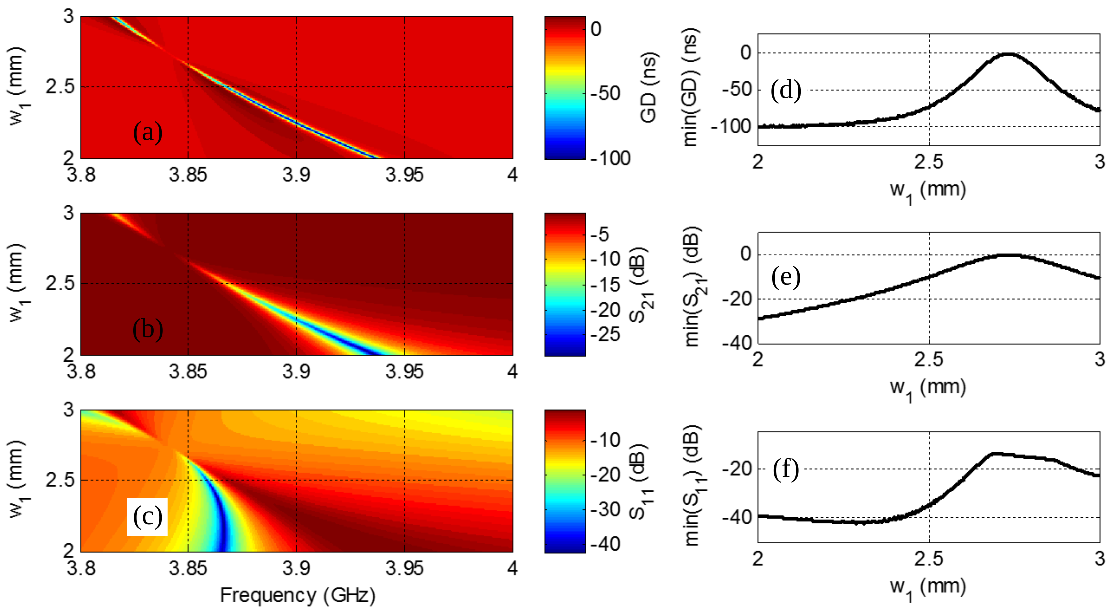

Figure 7. Mappings of (a) GD, (b) S_{21} and (c) S_{11} vs (f, w_1), and (d) min(GD), (e) min(S_{21}) and (f) min(S_{11}) vs w_1.

GD of Fig. 7(a). S_{21} decreases when w_1 varies from 2 mm to 2.7 mm and increases in the other range of w_1. The insertion loss is lower than 1 dB for $w_1 = 2.7$ mm and 2.8 mm as depicted in Fig. 7(e). Fig. 7(c) presents the S_{11} cartography. Fig. 7(f) shows that S_{11} is lower than -15 dB for w_1 between 2.2 mm and 3 mm.

4.2.2. Parametric Analysis with Respect to w_2

The present parametric analysis was performed with w_2 varied from 1 mm to 2 mm by 0.1 mm-step. The GD, S_{21}, and S_{11} responses are mapped in Fig. 8. Once again, the ladder topology behaves as a BP NGD function for all the considered values of w_2, as seen in Fig. 8(a). As depicted in Fig. 8(d), the NGD absolute value presents a minimum for w_2 around 1.8 mm.

The GD increases when w_2 varies from 1 mm to 1.8 mm and decreases when w_2 varies from 1.8 mm to 2 mm. In the range of w_2, Δf is about 6.2 MHz, and f_0 decreases with step around 22 MHz when w_2 increases. Fig. 8(b) represents the S_{21} mapping which reaches its maximum around 1.8 mm. As depicted in Fig. 8(e), S_{21} increases when w_2 varies from 1 mm to 1.8 mm and decreases when w_2 varies from 1.8 to 2 mm. Fig. 8(c) shows the S_{11} cartography which illustrates that the ladder circuit matching can be better than -10 dB in the considered range of w_2. As depicted in Fig. 8(f), S_{11} is better than -20 dB for w_2 between 1.3 and 2 mm.

4.2.3. Parametric Analysis with Respect to d_1

This third case study was carried out by linearly varying d_1 from 3 mm to 4.5 mm by 0.1 mm-step. Fig. 9 displays the GD, S_{21}, and S_{11} mappings versus (d_1, f). It can be observed in Fig. 9(a) that the ladder still behaves as a BP NGD function with bandwidth about 4 MHz, in the considered range of physical length d_1. The GD increases with d_1 as seen in Fig. 9(d). Moreover, the center frequency decreases from 4.472 GHz to 4.129 GHz. The mapping of Fig. 9(b) presents the S_{21} behavior with considerable similitude with GD of Fig. 9(a). S_{21} increases when d_1 varies from 3.5 mm to 4.5 mm as depicted in Fig. 9(e). Fig. 9(c) illustrates that the cartography of S_{11} is better when d_1 increases. This reflection coefficient is lower than -20 dB in the d_1 range as seen in Fig. 9(f).

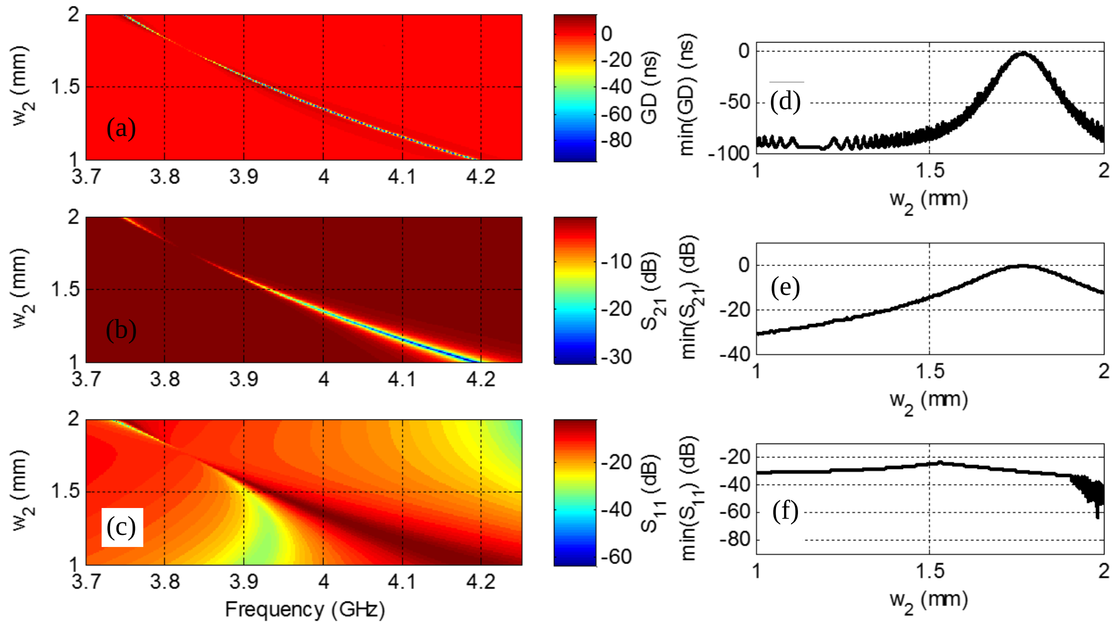

Figure 8. Cartographies of (a) GD, (b) S_{21} and (c) S_{11} vs (f, w_2), and (d) min(GD), (e) min(S_{21}) and (f) min(S_{11}).

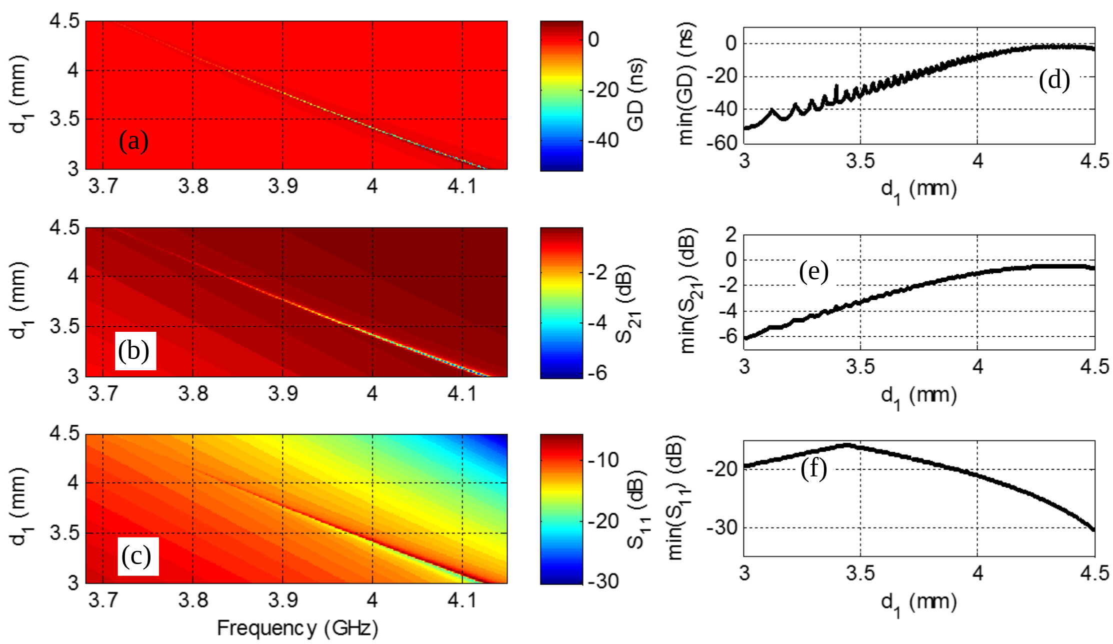

Figure 9. Cartographies of (a) GD, (b) S_{21} and (c) S_{11} vs (f, d_1), and (d) min(GD), (e) min(S_{21}) and (f) min(S_{11}) vs d_1.

4.2.4. Parametric Analyses with Respect to d_2

Figure 10 displays the GD, S_{21}, and S_{11} mappings versus (d_2, f) frequency. In this case, d_2 varies from 14 mm to 15 mm by 0.1 mm-step. As depicted in Fig. 10(a), the GD is negative in the entire simulated frequency band and d_2 range. It increases when d_2 varies from 14 mm to 15 mm. Moreover, the NGD bandwidth is about 4 MHz. and the NGD center frequency shifts to the low frequencies with a frequency

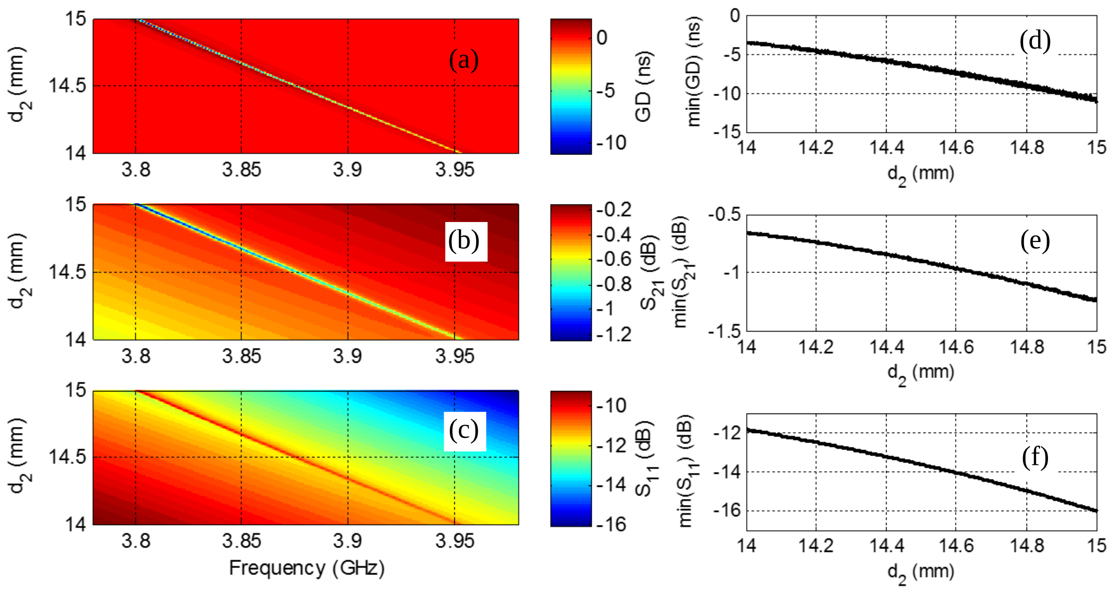

Figure 10. Cartographies of (a) GD, (b) S_{21} and (c) S_{11} vs (f, d_2), and (d) min(GD), (e) min(S_{21}), and (f) min(S_{11}).

step less than 21 MHz. The cartography of S_{21} in Fig. 10(b) shows how it increases with d_2. As depicted in Fig. 10(e), S_{21} is less than 2 dB in the range of d_2. Fig. 10(c) presents the S_{11} mapping. It can be seen that the reflection coefficient decreases when d_2 increases as illustrated in Fig. 10(f).

4.3. Simulated and Measured Validation Results

Design and simulation of the NGD ladder shape model were achieved with the RF/microwave electromagnetic commercial tool HFSS® from ANSOFT®. Experimental results were run with a Vector Network Analyzer (VNA) referenced R&S® ZNB40 (100 kHz–40 GHz). Figs. 11(a) and 11(b) illustrate the experimental setup of the ladder shape NGD prototype. The POC prototype has been implemented on an F4BK dielectric substrate characterized by relative permittivity $\varepsilon_r = 3.5$ and height $h = 1.27$ mm. Conductor lines are copper-metallized with thickness metallization, $t = 35\,\mu$m. Validation tests were realized between 3.52 GHz and 3.68 GHz. Figs. 11(c), 11(d), and 11(e) display GD, S_{21}, and S_{11} from simulations and measurements. The based TL elements 3D model designed on HFSS® is represented by the red curve and the measured prototype by the blue curve. One can note that simulation and measurements are well correlated. In Fig. 11(c), the Ladder structure behaves as a BP NGD circuit in the simulated and experimental frequency bands. It presents an NGD value of −3.5 ns around a 3.65 GHz NGD center frequency with a bandwidth around 37 MHz. Moreover, Figs. 11(d) and 11(e) show respectively that the transmission parameter S_{21} and reflection coefficient S_{11} are better than −5 dB and −8 dB respectively in the operating NGD bandwidth. Table 2 shows that the calculated, simulated, and measured NGD performances. Table 3 compares the NGD properties of the ladder

Table 2. Comparison of calculated, simulated and measured NGD performances of the tested circuit.

Solver	Theory	ADS®	Measurement
f_0	3.573 GHz	3.574 GHz	3.645 GHz
BW	20 MHz	20 MHz	37 MHz
GD_0	−3 ns	−3 ns	−3.5 ns
Computation time	1 ms	2.6 s	N/A

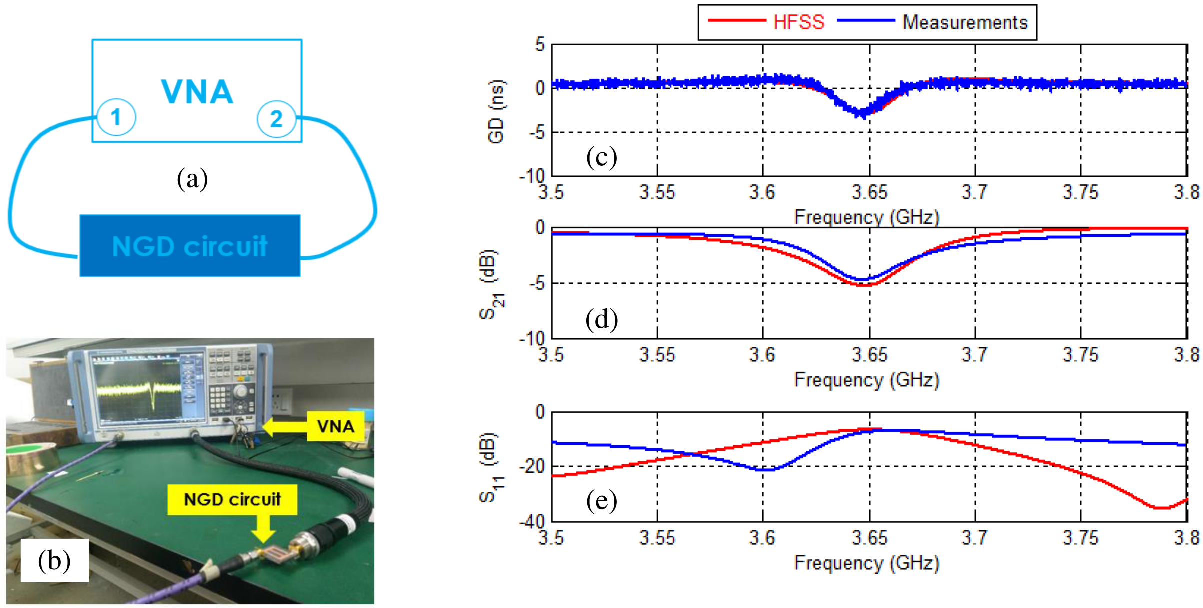

Figure 11. NGD circuit experimental setup: (a) diagram and (b) photograph. Comparison between calculated, simulated and measurements: (c) GD, (d) S_{21} and (e) S_{11}.

Table 3. NGD properties: Ladder shaped topology vs references NGD distributed circuit.

Distributed NGD topologies	GD (f_0) (ns)	NGD Bandwidth (MHz)	NGD Center frequency (GHz), f_0 (GHz)	$\mathrm{FoM_{NGD}}$
NGD Ladder Topology	-3.5	37	3.6	-0.1295
[42]	-2.3	20	1.26	-0.046
[34]	-7.7	35	1.79	-0.2695
[33]	-8.75	2.3	1.570	-0.02013

shaped topology with some references NGD distributed ones by defining the figure-of-merit as:

$$\mathrm{FoM_{NGD}} = \mathrm{GD}(f_0) \times \Delta f. \tag{32}$$

One can remark that the NGD ladder topology operates at a higher NGD frequency and a greater bandwidth than these referenced NGD circuits.

5. CONCLUSION

Innovative functions are necessary to increase the future communication system performances. In this rapidly changing technology, the BP NGD function is expected to be a good candidate for the microwave signal integrity enhancement. The present study develops a design and model of the innovative ladder-shape topology. The structure understudy is composed of TL elements. The topological analysis is elaborated with the TL element equivalent S- and Z-matrix under characteristic impedance and propagation constant consideration. Then the NGD distributed circuit is simulated with the RF/microwave electromagnetic tool HFSS® and compared with the POC prototype measurements. The obtained results highlight the ladder shaped circuit BP NGD function. An NGD performance of -3.5 ns GD value and 3.63 GHz central frequency over 40 MHz bandwidth is obtained from the simulation and measurements. Parametric analyses with respect to the TL physical parameters of the BP NGD ladder structure were discussed to observe the influence on NGD value and central frequency.

The proposed BP NGD function promises some innovative RF and microwave devices in the future. Compared to the classical electronic functions, the NGD circuits present the following main advantages:

- The NGD function is only the one electronic function enabling to cancel out via equalization of delay effect in the communication system [7, 8, 14, 15].
- The NGD function allows to improve in challenging way the antenna performances [15–17, 21, 22].
- The NGD function has a unique possibility to design non-Foster elements [23].
- The NGD function enables to design ideally zero ideally independent frequency phase shifters [15, 24].

REFERENCES

1. "5 critical 5G network deployment challenges — Infovista," https://www.infovista.com/blog/5g-network-deployment-challenges (consulté le févr. 13, 2021).
2. "5G-PPP," https://5g-ppp.eu/(consulté le févr. 13, 2021).
3. R. & S. International, "R&S®Cloud4Testing: 5G signal analysis," https://www.rohde-schwarz.com/fr/produits/test-et-mesure/analyseurs-de-signaux-et-de-spectres/digital-products/cloud4testing/cloud4testing-5g-application-package_253876.html (consulté le févr. 13, 2021).
4. Agrawal, G., S. Aniruddhan, and R. K. Ganti, "Multi-band RF time delay element based on frequency translation," *2014 IEEE International Symposium on Circuits and Systems (ISCAS)*, 1368–1371, 2014.
5. Myoung, S.-S., B.-S. Kwon, Y.-H. Kim, and J.-G. Yook, "Effect of group delay in RF BPF on impulse radio systems," *IEICE Trans. Commun.*, Vol. 90, No. 12, 3514–3522, 2007.
6. Groenewold, G., "Noise and group delay in active filters," *IEEE Trans. Circuits Syst. Regul. Pap.*, Vol. 54, No. 7, 1471–1480, 2007.
7. Shao, T., Z. Wang, S. Fang, H. Liu, and Z. N. Chen, "A full-passband linear-phase band-pass filter equalized with negative group delay circuits," *IEEE Access*, Vol. 8, 43336–43343, 2020.
8. Shao, T., Z. Wang, S. Fang, H. Liu, and Z. N. Chen, "A group-delay-compensation admittance inverter for full-passband self-equalization of linear-phase band-pass filter," *AEU-Int. J. Electron. Commun.*, Vol. 123, 153297, 2020.
9. Kandic, M. and G. E. Bridges, "Asymptotic limits of negative group delay in active resonator-based distributed circuits," *IEEE Trans. Circuits Syst. Regul. Pap.*, Vol. 58, No. 8, 1727–1735, 2011.
10. Wu, C.-T. M. and T. Itoh, "Maximally flat negative group-delay circuit: A microwave transversal filter approach," *IEEE Trans. Microw. Theory Tech.*, Vol. 62, No. 6, 1330–1342, 2014.
11. Markley, L. and G. V. Eleftheriades, "Quad-band negative-refractive-index transmission-line unit cell with reduced group delay," *Electron. Lett.*, Vol. 46, No. 17, 1206–1208, 2010.
12. Barroso, J. J., J. E. B. Oliveira, O. L. Coutinho, and U. C. Hasar, "Negative group velocity in resistive lossy left-handed transmission lines," *IET Microwaves, Antennas & Propagation*, Vol. 10, No. 7, 808–815, May 2016.
13. Awwad, F. R., M. Nekili, V. Ramachandran, and M. Sawan, "On modeling of parallel repeater-insertion methodologies for SoC interconnects," *IEEE Trans. Circuits Syst. Regul. Pap.*, Vol. 55, No. 1, 322–335, 2008.
14. Ravelo, B., "Recovery of microwave-digital signal integrity with NGD circuits," *Photon Optoelectron*, Vol. 2, No. 1, 8–16, 2013.
15. Xiao, J.-K., Q.-F. Wang, and J.-G. Ma, "Negative group delay circuits and applications: Feedforward amplifiers, phased-array antennas, constant phase shifters, non-foster elements, interconnection equalization, and power dividers," *IEEE Microwave Magazine*, Vol. 22, No. 2, 16–32, Feb. 2021.

16. Abdulkarim, Y. I., H. N. Awl, F. F. Muhammadsharif, M. Karaaslan, R. H. Mahmud, S. O. Hasan, Ö. Işık, H. Luo, and S. Huang, "A low-profile antenna based on single-layer metasurface for Ku-band applications," *International Journal of Antennas and Propagation*, Vol. 2020, Article ID 8813951, 8 pages, 2020.
17. Akgol, O., O. Altintas, E. Unal, et al., "Linear to left-and right-hand circular polarization conversion by using a metasurface structure," *Int. Journal of Microwave and Wireless Technologies*, Vol. 10, No. 1, 133–138, 2008.
18. Altıntaş, O., M. Aksoy, E. Ünal, M. Karaaslan, and C. Sabah, "Operating frequency reconfiguration study for a split ring resonator based microfluidic sensor," *J. Electrochem. Soc.*, Vol. 167, No. 14, 147512, Nov. 2020.
19. Bakır, M., S. Dalgaç, M. Karaaslan, F. Karadag, O. Akgol, E. Unal, T. Depçi, and C. Sabah, "A comprehensive study on fuel adulteration sensing by using triple ring resonator type metamaterial," *J. Electrochem. Soc.*, Vol. 166, B1044–B1052, 2019.
20. Velez, P., L. Su, K. Grenier, J. Mata-Contreras, D. Dubuc, and F. Martin, "Microwave microfluidic sensor based on a microstrip splitter/combiner configuration and split ring resonators (SRRs) for dielectric characterization of liquids," *IEEE Sens. J.*, Vol. 17, 6589–6598, 2017.
21. Mirzaei, H. and G. V. Eleftheriades, "Arbitrary-angle squint-free beamforming in series-fed antenna arrays using non-foster elements synthesized by negative-group-delay networks," *IEEE Trans. Antennas Propag.*, Vol. 63, No. 5, 1997–2010, May 2015.
22. Zhu, M. and C.-T. M. Wu, "Reconfigurable series feed network for squint-free antenna beamforming using distributed amplifier-based negative group delay circuit," *2019 49th European Microwave Conference (EuMC)*, 256–259, 2019.
23. Zhang, T., R. Xu, and C.-T. M. Wu, "Unconditionally stable non-foster element using active transversal-filter-based negative group delay circuit," *IEEE Microw. Wirel. Compon. Lett.*, Vol. 27, No. 10, 921–923, 2017.
24. Ravelo, B., "Distributed NGD active circuit for RF-microwave communication," *AEU-Int. J. Electron. Commun.*, Vol. 68, No. 4, 282–290, 2014.
25. Ravelo, B., "Delay modeling of high-speed distributed interconnect for the signal integrity prediction," *Eur. Phys. J. Appl. Phys.*, Vol. 57, No. 3, 31002, 2012.
26. Ravelo, B., "Similitude between the NGD function and filter gain behaviours," *Int. J. Circuit Theory Appl.*, Vol. 42, No. 10, 1016–1032, 2014.
27. Ravelo, B., "On low-pass, high-pass, bandpass, and stop-band NGD RF passive circuits," *URSI Radio Sci. Bull.*, Vol. 2017, No. 363, 10–27, 2017.
28. Wu, C.-T. M., S. Gharavi, and T. Itoh, "Negative group delay circuit based on a multisection asymmetrical directional coupler," *2013 Asia-Pacific Microwave Conference Proceedings (APMC)*, 333–334, 2013.
29. Qiu, L.-F., L.-S. Wu, W.-Y. Yin, and J.-F. Mao, "Absorptive bandstop filter with prescribed negative group delay and bandwidth," *IEEE Microw. Wirel. Compon. Lett.*, Vol. 27, No. 7, 639–641, Jul. 2017.
30. Chaudhary, G., Y. Jeong, and J. Lim, "Miniaturized dual-band negative group delay circuit using dual-plane defected structures," *IEEE Microw. Wirel. Compon. Lett.*, Vol. 24, No. 8, 521–523, 2014.
31. Chaudhary, G. and Y. Jeong, "Low signal-attenuation negative group-delay network topologies using coupled lines," *IEEE Trans. Microw. Theory Tech.*, Vol. 62, No. 10, 2316–2324, 2014.
32. Chaudhary, G. and Y. Jeong, "Transmission-type negative group delay networks using coupled line doublet structure," *IET Microw. Antennas Propag.*, Vol. 9, No. 8, 748–754, 2015.
33. Shao, T., Z. Wang, S. Fang, H. Liu, and S. Fu, "A compact transmission-line self-matched negative group delay microwave circuit," *IEEE Access*, Vol. 5, 22836–22843, 2017, doi: 10.1109/ACCESS.2017.2761890.
34. Liu, G. and J. Xu, "Compact transmission-type negative group delay circuit with low attenuation," *Electron. Lett.*, Vol. 53, No. 7, 476–478, févr, 2017, doi: 10.1049/el.2017.0328.

35. Shao, T., S. Fang, Z. Wang, and H. Liu, "A compact dual-band negative group delay microwave circuit," *Radioengineering*, Vol. 27, No. 4, 1070–1076, Sept. 2018, doi: 10.13164/re.2018.1070.
36. Ravelo, B. and F. Wan, "NGD synthesizer with feedback hybrid coupler," *2019 IEEE Radio and Antenna Days of the Indian Ocean (RADIO)*, 1–2, Sept. 2019, doi: 10.23919/RADIO46463.2019.8968893.
37. Ravelo, B., "Hybrid coupler-based NGD circuit," *Negat. Group Delay Devices Concepts Appl.*, 147–172, Nov. 2018, doi: 10.1049/PBCS043E_ch5.
38. Wu, C. M., S. Gharavi, and T. Itoh, "Negative group delay circuit based on a multisection asymmetrical directional coupler," *2013 Asia-Pacific Microwave Conference Proceedings (APMC)*, 333–334, Nov. 2013, doi: 10.1109/APMC.2013.6695137.
39. Wu, C. M. and T. Itoh, "Maximally flat negative group-delay circuit: A microwave transversal filter approach," *IEEE Trans. Microw. Theory Tech.*, Vol. 62, No. 6, 1330–1342, Jun. 2014, doi: 10.1109/TMTT.2014.2320220.
40. Hammerstad, E. and O. Jensen, "Accurate models for microstrip computer-aided design," *1980 IEEE MTT-S International Microwave Symposium Digest*, 407–409, 1980.
41. Frickey, D. A., "Conversions between S, Z, Y, H, ABCD, and T parameters which are valid for complex source and load impedances," *IEEE Trans. Microw. Theory Tech.*, Vol. 42, No. 2, 205–211, 1994.
42. Ravelo, B., "Theory of coupled line coupler-based negative group delay microwave circuit," *IEEE Trans. Microw. Theory Tech.*, Vol. 64, No. 11, 3604–3611, Nov. 2016, doi: 10.1109/TMTT.2016.2604316.